Lower Crustal Seismicity on the Eastern Border Faults of the Main Ethiopian Rift

Enter authors here: Sacha Lapins[1], J-Michael Kendall[2], Atalay Ayele[3], Matthew Wilks[1], Andy Nowacki[4], and Katharine V Cashman[1].

[1]School of Earth Sciences, University of Bristol, UK.

[2]Department of Earth Sciences, University of Oxford, UK.

[3]Institute of Geophysics, Space Science and Astronomy, Addis Ababa University, Ethiopia.

[4]School of Earth and Environment, University of Leeds, UK.

Corresponding author: Sacha Lapins (sacha.lapins@bristol.ac.uk)

Key Points:

- A sequence of lower crustal seismicity is identified 30km east of Corbetti caldera on the eastern border faults of the Main Ethiopian Rift
- Mixture distributions are used to overcome misinterpretations from large uncertainty in individual event locations
- Spatial and temporal characteristics indicate that the source of this seismicity relates to fluid or magmatic processes

Abstract

Lower crustal seismicity is commonly observed in continental rift zones despite the crust at such depths being ductile enough to prohibit brittle failure. The source of such deep seismicity across the East African Rift remains an outstanding question. Here we present analysis of an isolated cluster of lower crustal earthquakes located on the eastern border faults of the Main Ethiopian Rift, near the Corbetti caldera. Lower crustal earthquakes have not previously been observed in this area. Phase arrival times were determined using an automated picking approach based on continuous wavelet transform and statistical changepoint detection methods. We overcome misinterpretations from large hypocentre depth errors by considering mixture distributions for all events and their associated uncertainties. These mixture distributions represent probability density functions of any event occurring at a given depth. The mixture distribution mode for a variety of different velocity models and error parameters remained stable at a depth of 28 – 32 km, with the vast majority of maximum likelihood estimates for individual hypocenters located at depths of 25 – 35 km. Most events occur over a two-month period, with 90% of cumulative seismic moment occurring during March and April 2012. The ephemeral and localized nature of this seismicity, combined with low event magnitudes and regional hydrothermal / magmatic activity, all suggest that these lower crustal events are likely related to fluid or magmatic processes. Plausible mechanisms include the movement of magma and/or exsolution of volatiles at depth causing transient high strain rates and pore fluid pressures that induce seismicity.

Plain Language Summary

-

1 Introduction

Seismicity associated with continental rift zones can reach depths of more than 30 km (e.g., Albaric et al., 2014; Keir et al., 2009; Reyners et al., 2007; Yang & Chen, 2010) despite the general conception that the crust at such depths is too ductile for brittle failure to occur (Chen & Molnar, 1983). In the East African Rift (EAR; Fig 1), deep crustal, and even upper mantle, seismicity has been observed along the younger eastern and western branches of the EAR (Albaric et al., 2014; Lavayssière, Drooff, et al., 2019; Lindenfeld & Rümpker, 2011; Nyblade & Langston, 1995; Yang & Chen, 2010), as well as beneath the western margins of the more well-developed, magmatic Main Ethiopian Rift (MER) at the northern end of the of the EAR (Keir et al., 2009; Fig 1). One explanation is that these earthquakes are caused by slip on border faults into relatively cold or strengthened lower crust (Doser & Yarwood, 1994; Jackson & Blenkinsop, 1993; Zhao et al., 1997). Such an explanation requires the underlying mantle to be cool and/or strong enough for earthquakes to occur, for which there may be compelling evidence beneath less magmatic segments on the western branch of the EAR (Lindenfeld & Rümpker, 2011; Yang & Chen, 2010). However, beneath the considerably more magmatic MER, where the lithospheric mantle has high enough temperatures to sustain partial melt (Kendall et al., 2005; Hammond et al., 2014), the lower crust and upper mantle are deemed too ductile for brittle failure; here deep seismicity is thought to be induced by magmatic processes and fluids (Keir et al., 2009; Reyners et al., 2007; Soosalu et al., 2010). In other oceanic and continental rift settings, such as Iceland and the Taupo rift in New Zealand, deep seismicity has been associated with high strain rates / pore pressures (e.g, Greenfield & White, 2015; Soosalu et al., 2010; White et al., 2011), magma/fluid emplacement (Smith et al., 2016) and the weakening of border faults (e.g., Reyners et al., 2007) arising from melt movement and/or the exsolution of volatiles. However, the mechanism for deep seismicity in the EAR, where the level of magmatism varies from section to section, is still debated (e.g., Weinstein et al., 2017).

In this paper, we examine an isolated cluster of lower-crustal seismicity approximately 30 km east of the Corbetti caldera on the eastern border faults of the MER, where no previous lower crustal seismicity has been observed. The distribution mode of this seismicity lies at a depth of 28 – 32 km, directly beneath the Wondo Genet scarp (Fig 2). This scarp is thought to relate to an intersection between the rift border and the easternmost end of a cross-cutting fault structure that pre-dates the rift (Lloyd, Biggs, Wilks, et al., 2018; Fig 2), with the interaction of these two faults potentially influencing seismicity in the area. We determine event phase-arrival times with high precision using wavelet transform and statistical changepoint detection methods. We attempt to reduce the variability of individual event locations, largely caused by poor seismic array coverage relative to the region of seismicity, by considering the mixture distribution of all events observed for a given velocity model and set of location algorithm parameters. The temporal and spatial distribution of these events suggests that these isolated events may be caused by a single, ephemeral intrusion at lower crustal depths that causes overpressure, inducing seismicity, or hot fluids reducing the effective normal stress on the faults.

2 The Main Ethiopian Rift (MER) and Corbetti Caldera

The MER is an area of continental rifting that forms the major divergent plate boundary between the Nubian and Somalian tectonic plates at the northern end of the EAR (Fig 1). It is thought to have initiated and developed asynchronously along its length (e.g., Wolfenden et al., 2004), with the development of different sectors influencing magmatism, strain and crustal thickness across the region (Keir et al., 2015; Muluneh et al., 2017). Most regional seismicity occurs along the axis of the MER (Wilks, 2016), where the seismogenic layer is constrained to upper crustal depths (< ~ 16 km; Muluneh et al., 2018). However, earthquakes as deep as ~ 35 km (the approximate thickness of the crust in this region; Dugda et al., 2005; Ebinger et al., 2017; Stuart et al., 2006) have been identified on the western margin of the MER, associated with areas of recent volcanism along the Debre-Zeit and Yerer-Tullu Wellel Volcanotectonic Lineaments near Addis Ababa (Keir et al., 2009). Additional lower crustal seismicity at depths of ~ 22 km, which is still below the Brittle-Ductile Transition (BDT) zone for the region (16km depth; Muluneh et al., 2018), has been observed beneath the rift-adjacent north-western (NW) Ethiopian Plateau (Keir et al., 2009), north of Addis Ababa. The location of this seismicity in volcanic areas supports the idea of magma emplacement below/into the lower crust as a source of lower crustal seismicity in the MER (e.g., Keir et al., 2009; Soosalu et al., 2010), rather than fault slip within a relatively cold or strengthened lower crust.

The Corbetti caldera is the southernmost silicic center along the rift. It lies toward the eastern side of the MER and formed at 182 +/- 18 ka (Lloyd, Biggs, Wilks, et al., 2018). Its magmatic and hydrothermal processes are thought to be influenced by a cross-cutting fault structure that pre-dates the rift and may extend as far as the rift border, ~ 30 km to the east (Lloyd, Biggs, Wilks, et al., 2018). Seismicity beneath the caldera appears to be constrained to the uppermost crust (Lavayssière, Greenfield, et al., 2019; Lloyd, Biggs, Birhanu, et al., 2018), although previous seismic monitoring in the area has been limited.

Prior to the events analyzed in this paper, no other sequence of lower crustal seismicity had been observed beneath the rift itself, the Corbetti caldera, the eastern border faults of the MER, or the seismically quiet south-eastern (SE) Somalian plateau to the east.

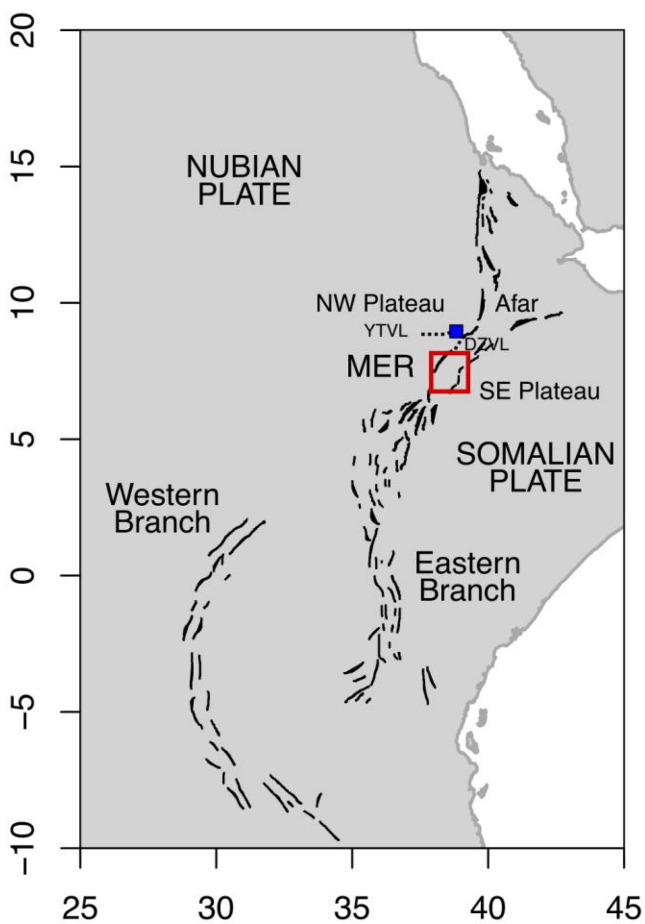

Figure 1 – Map of East African Rift (EAR) with schematic rift-bounding faults after Foster and Jackson (1998). Horizontal and vertical axes show longitude and latitude, respectively. Blue square is Addis Ababa. Red box is

location of map in Figure 2. Previous lower crustal seismicity has been observed along less magmatic sections of the western and eastern branches of the EAR to the south, as well as beneath the Debre-Zeit and Yerer-Tullu Wellel Volcanotectonic Lineaments (DZVL, dotted line southeast of Addis Ababa, and YTVL, dotted line west of Addis Ababa, respectively) on the western margins of the Main Ethiopian Rift (MER).

3 Seismic Array Geometry

Two local seismic arrays were deployed at Aluto (Wilks et al., 2017) and Corbetti (Wilks, 2016) volcanoes throughout 2012 and 2013, with 12 and 7 broadband seismometers, respectively, deployed at each volcano, although only subsets of around 15 of these instruments were operational at any given time throughout the study period (Fig 2). The relative location of these two local arrays to the observed seismicity leaves a substantial array gap (~ 270 degrees), with no other regional seismic networks operating at the time.

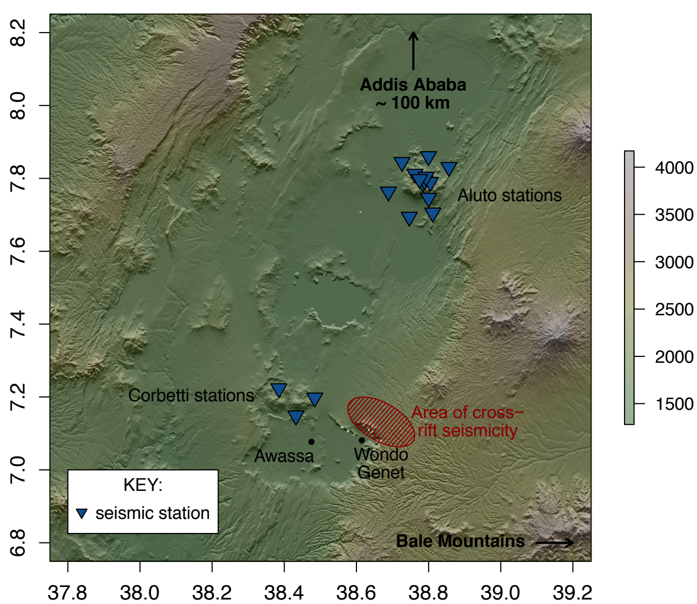

Figure 2 – Map of available instruments from Corbetti and Aluto volcano seismic arrays, with general area of analyzed seismicity highlighted around 30 km to the east of Corbetti. Map color denotes surface altitude in meters above sea level. Horizontal and vertical axes show longitude and latitude, respectively.

4 Phase Arrival Picking

Phase arrival times were identified manually across the full deployment (> 3000 events over 2 years continuous data; Wilks, 2016). The anomalous subset of apparent lower crustal seismicity was identified by subsequent event location (number of events = 134). Initial phase arrival picks for this subset had large pick errors and large predicted travel-time (TT) residuals, sometimes on the order of several seconds; for this reason, the first step in this study was to reduce this source of error in hypocentre estimation through a time-frequency-based automated picking approach (Figs 3 and 4). This approach was based on continuous wavelet transform (CWT) spectral analysis (e.g., Lapins et al., 2020) and statistical changepoint detection (Fryzlewicz, 2014).

P-wave arrivals were characterized by producing CWT scalograms between 2 and 12 Hz (e.g., Lapins et al., 2020; Fig 3b) for the raw vertical component traces at each station (Fig 3a). We then determined the average wavelet energy between these frequency bounds for each time sample point (black line in Fig 3c) using both low- and standard-frequency Morlet wavelets (Morlet central frequency parameter $\boldsymbol{\omega_0 = 1}$ and $\boldsymbol{\omega_0 = 6}$, respectively). Changes in average wavelet energy with time were detected using Wild Binary Segmentation (WBS; Fryzlewicz, 2014), an *a posteriori* changepoint detection method that segments the signal by a given statistical property, which in this case is mean energy. The WBS ‘threshold’ parameter for determining a change in mean energy was set very low (threshold constant $\boldsymbol{c = 0.5}$), which led to a near-uniform rate of ‘false positive’ changepoint detections during pre-event noise (1 – 2 detections per second) and a much higher rate of changepoint detections at the P-wave arrival and during the coda (>> 1 detection per second; vertical red lines in Fig 3c). The cumulative number of detected changepoints within a signal window (90 s) was then used to identify P-wave arrival through second-order differencing (lag = 4 s) and a simple trigger algorithm (Fig 3d).

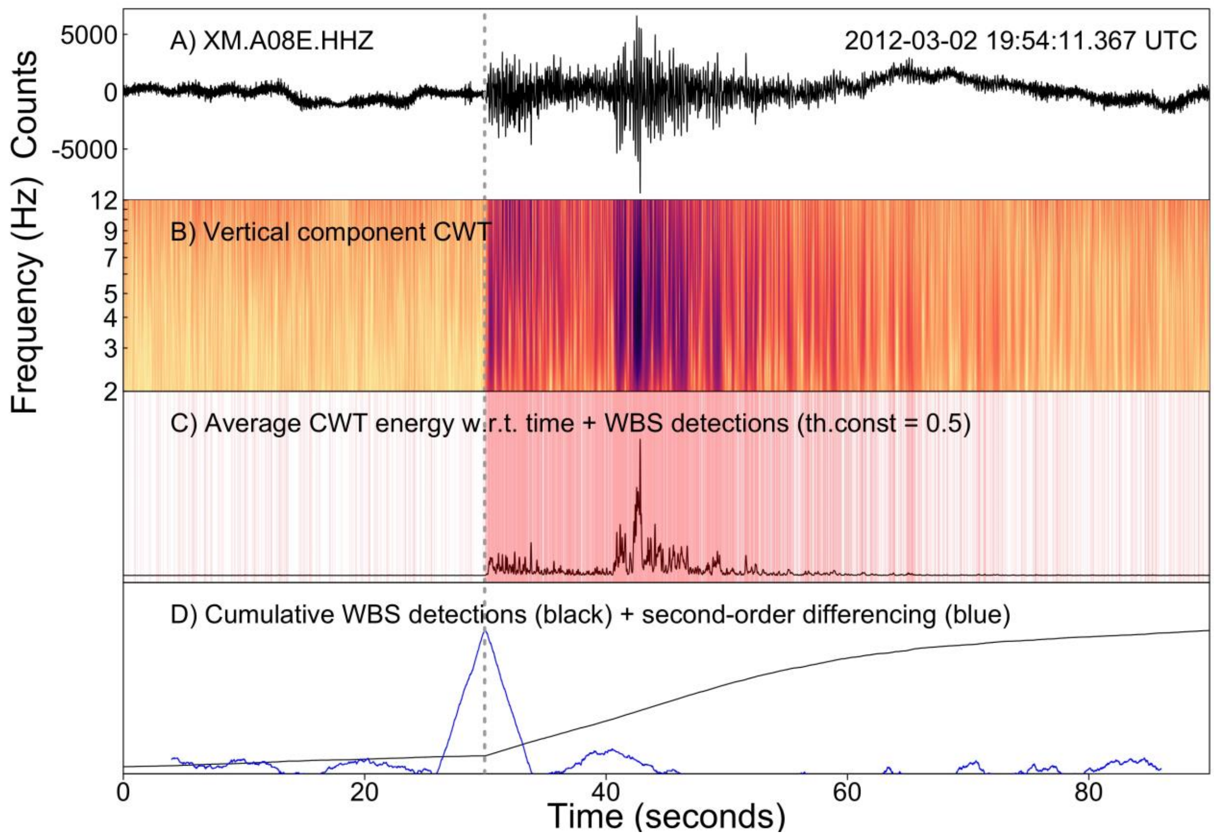

Figure 3 – A) Raw vertical component trace; B) CWT scalogram between 2 and 12 Hz for trace above (Morlet wavelet with central frequency $\boldsymbol{\omega_0 = 1}$); C) Average wavelet energy (black line) with WBS changepoint detections marked with semi-transparent red lines; D) Cumulative number of WBS detections (black line) with second-order differencing (lag = 4 s; blue line) – sharp blue peak and dashed grey line indicate determined P-wave arrival time.

S-wave arrivals were identified in a similar manner to P-wave arrivals but using the cross-wavelet transform (XWT) derived from the two horizontal component CWT scalograms at each station (Fig 4). This had the effect of reducing incoherent background noise while enhancing coherent signal across the two horizontal components (Fig 4b). Again, the average wavelet energy was determined at each time sample point for low- and standard-frequency Morlet wavelets. Finally, WBS and second-order differencing was used to identify S-wave arrivals common to both horizontal components (Figs 4c and d), this time with a greater WBS threshold constant ($\boldsymbol{c = 250}$ for Aluto stations, $\boldsymbol{c = 5000}$ for nearby Corbetti stations) to avoid a higher rate of changepoint detections around P-wave arrivals. We use different threshold constants across the two arrays due to higher amplitude values in the raw signal at the nearer Corbetti stations.

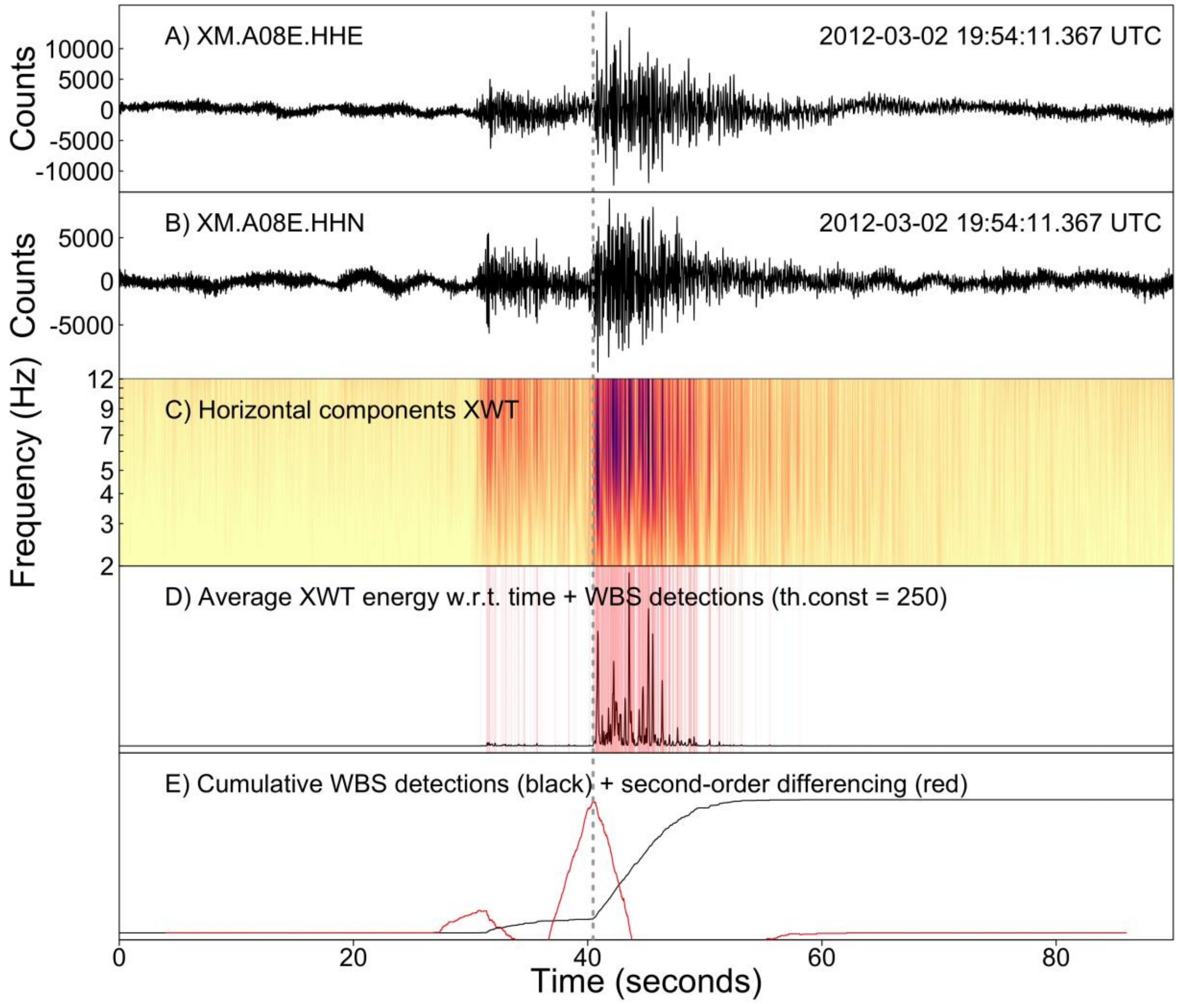

Figure 4 – A) Raw EW horizontal component trace; B) Raw NS horizontal component trace; C) Cross wavelet transform (XWT) scalogram between 2 and 12 Hz for both horizontal components (Morlet wavelet with central frequency $\omega_0 = 1$); D) Average XWT energy (black line) + WBS changepoint detections marked with semi-transparent red lines; E) Cumulative number of WBS detections (black line) and double-differenced cumulative number of WBS detections (lag = 4 s; red line). Sharp red peak and dashed grey line indicate determined S-wave arrival time.

All P- and S-wave picks were manually checked against raw and filtered traces, CWT scalogram images and additional STA/LTA (e.g., Withers et al., 1998) traces to assess quality and uncertainty. Arrival times for highly emergent signals were sometimes picked late by the CWT-WBS approach outlined above, likely a consequence of the lower frequency onset of these signals, which is outside of the frequency range encompassed by the CWT scalograms (2 – 12 Hz). These arrival times were adjusted manually using visual determination on wider frequency band CWT scalograms and raw traces. Arrival time picks that were difficult to confirm manually (e.g., in the presence of very low signal-noise ratio, SNR) were removed.

Picks made using the low-frequency Morlet wavelet ($\boldsymbol{\omega_0} = \mathbf{1}$), which yields improved time resolution at the cost of frequency resolution (Addison et al., 2002; Lapins et al., 2020), were more accurate for signals with medium to high SNR, whilst picks based on the standard Morlet wavelet ($\boldsymbol{\omega_0} = \mathbf{6}$) were more accurate for very noisy signals because of greater frequency localization of pertinent signal features among ambient noise (Lapins et al., 2020).

5 Absolute Event Locations

Events were located using NonLinLoc (Lomax et al., 2000) and three different regional velocity models (Daly et al., 2008; Mackenzie et al., 2005; details in Fig 5 caption); travel-time error was varied to assess the stability of event locations and determine potential bias in absolute hypocentre locations (e.g., artificially deep locations). Only events with a total of seven or more phase arrival times, including at least one S phase, were located (58 events in total). We include at least one S phase to improve spatial constraints on hypocentre locations (e.g., Lomax et al., 2009), which can have large uncertainties when using stations with a large array gap or that are far from the event.

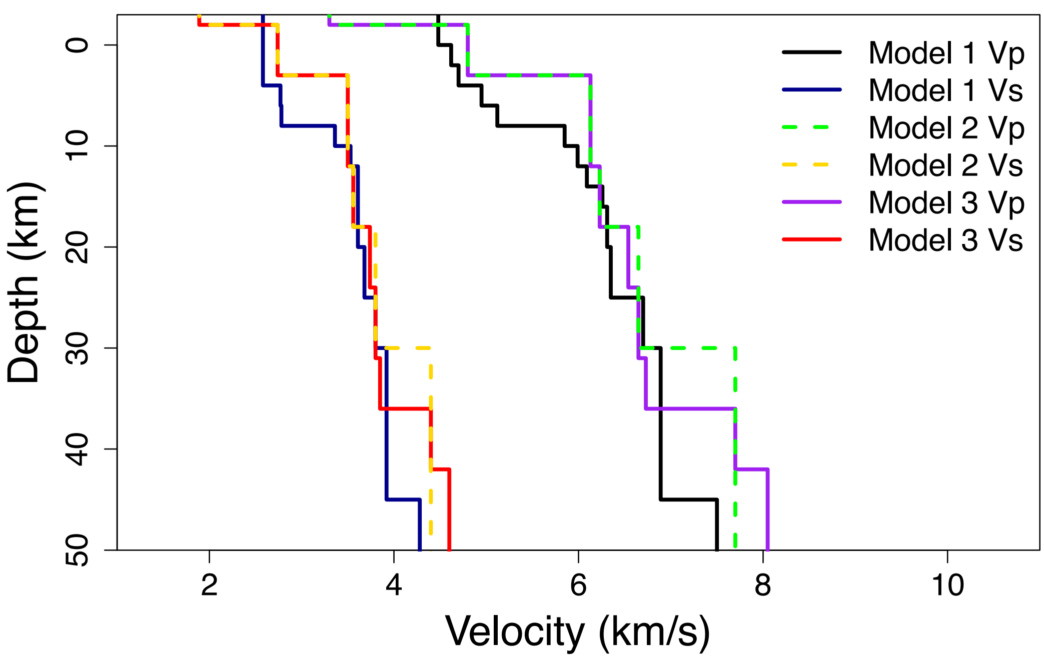

Figure 5 – Velocity models used for locating events (Vp = P-wave velocity; Vs = S-wave velocity). Model 1 is from Table 1 in Daly et al. (2008); Model 2 is approximated from Fig 5 in Daly et al. (2008); Model 3 is approximated from Fig 6 in Mackenzie et al. (2005). Vp/Vs ratio of 1.75 (average from Table 1 in Daly et al., 2008) used for Models 2 and 3 as only Vp given in original publications.

The significant array gap in this case (approximately 270 degrees) meant that individual event locations did indeed have large error distributions, although deeper events were generally better constrained than shallower events (Fig 6). For this reason, we also examine mixture distributions (a weighted combination of probability distributions for each individual event location) for all events, with a given set of location parameters (Fig 7), to determine stability and likelihood of event depth estimates using the whole population of events in the study. More formally, a (finite) mixture distribution, f, is a convex combination of n component probability distributions, $p_1(\boldsymbol{x})$, …, $p_n(\boldsymbol{x})$,

$$f(\boldsymbol{x}) = \sum_{i=1}^{n} w_i p_i(\boldsymbol{x}), \tag{1}$$

with weights $\boldsymbol{w_1}$, …, $\boldsymbol{w_n}$ such that $\boldsymbol{w_i} \geq \boldsymbol{0}$ and $\sum \boldsymbol{w_i} = \boldsymbol{1}$. Here, the component distributions, $\boldsymbol{p_i(x)}$, are the individual posterior probability density functions (PDFs) for each event's hypocentre location, estimated by NonLinLoc, where the vector $\boldsymbol{x}$ represents the three-dimensional spatial x, y, z hypocentre location and $\boldsymbol{i}$ is event index $\boldsymbol{1, \ldots, n}$. A mixture distribution preserves the required properties of probability distributions (non-negativity and integrating to 1) and is therefore itself a probability distribution.

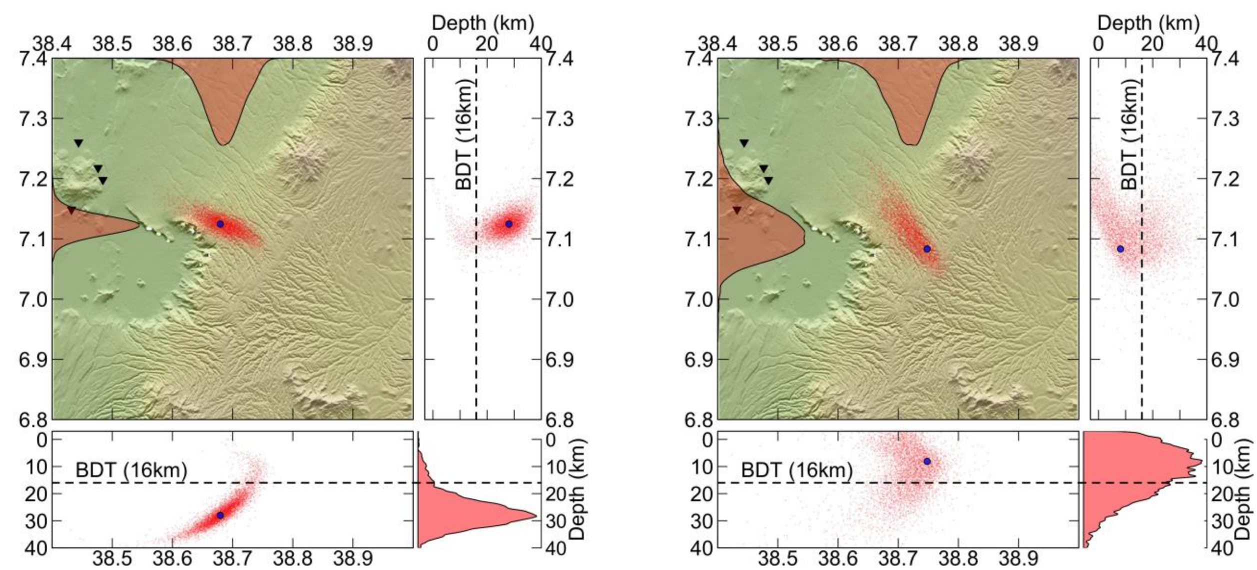

Figure 6 – Examples of individual event locations from NonLinLoc. Left: example of 'well-constrained' deep event – depth error estimates (red scatter and density curves) are quite large, spanning ~ 20 km depth, although clearly below the BDT and far more compact than those for shallow events. Right: an example of a 'typical' shallow event – red scatter and density curves representing error estimates are more diffuse and multimodal, suggesting greater uncertainty in event location. Red scatter and density curves are comprised of 5,000 samples drawn from the posterior PDF for each event hypocentre location.

We use mixture distributions to estimate the overall population distribution for all event locations and assess the likelihood of events occurring at a given depth (from here on we use the terms *overall population distribution* and *mixture distribution* interchangeably). In practice, probability distributions for individual earthquake locations are nonlinear and may be mathematically intractable. For this reason, earthquake location distributions are often estimated through probabilistic sampling of their complete posterior distribution (e.g., Gesret et al., 2015; Lomax et al., 2000). The number of samples used for estimating each component distribution is determined by its corresponding weight with regards to the mixture distribution (Eq. 1). As each component distribution in our study represents a single event location, all with equal weight, all component distributions are weighted equally, with the same number of samples drawn from each event location PDF in NonLinLoc ($s_i = 5000$, where s_i is the number of samples drawn for event index $i = 1, \ldots, n$).

Residuals between observed and expected travel times were greatly improved over initial manual picking through the CWT-WBS picking approach outlined in Section 4 (original manual-picking mean absolute travel-time residuals = 0.89 s; CWT-WBS mean absolute travel-time residuals = 0.23 s). However, reducing pick error did not markedly reduce the size of individual event location uncertainties and, in some cases, using a smaller number of higher confidence phase arrival times produced greater hypocentre location uncertainty (in terms of spatial spread) than using a larger number of lower confidence arrival times. This suggests that arrival time pick error has a smaller contribution to absolute location uncertainty in NonLinLoc than array geometry and estimates of travel time and velocity model error (Lomax et al., 2009). Despite the large uncertainty in individual event locations, the overall population (mixture) distribution for all event locations produces a clear, stable mode between 28 and 32 km depth for all velocity models and model error parameters (shaded density curves in Fig 7). Furthermore, the vast majority of event hypocenters are located between depths of 25 – 35 km (histograms in Fig 7) for any given level of Gaussian travel time error. This suggests that most events are indeed at lower crustal depths, although this becomes understandably less clear with very large travel time error levels (e.g., ≥ 10 % travel time error; Fig 7 bottom). The maximum likelihood estimates for hypocentre locations across all model runs also fall into two distinct clusters: a small, shallower cluster above the BDT zone (Muluneh et al., 2018) and a larger, deeper cluster between depths of 20 – 35 km (Fig 7), with very few events located around the BDT zone itself.

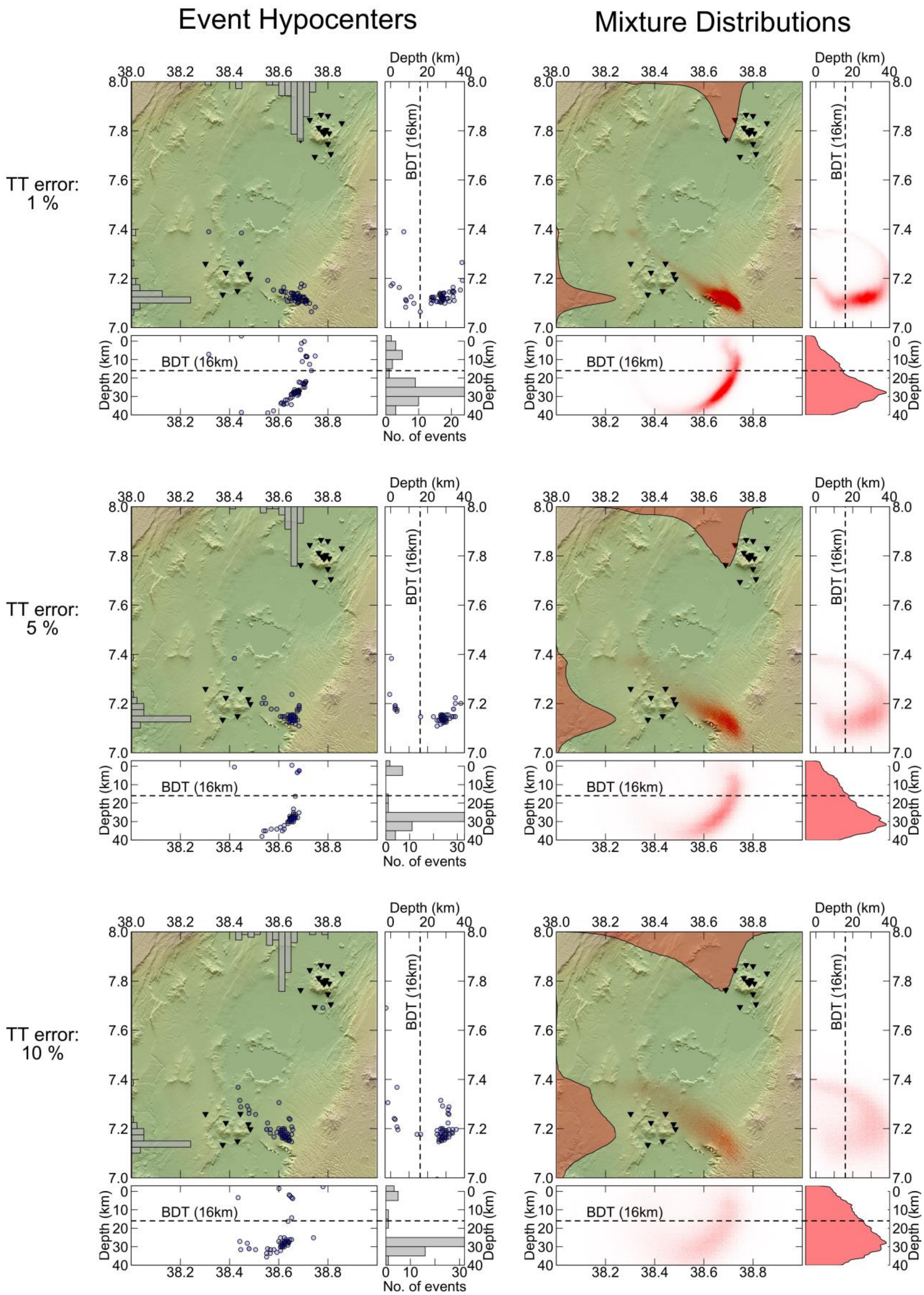

Event Hypocenters
Mixture Distributions
TT error: 1 %
TT error: 5 %
TT error: 10 %
Depth (km)
BDT (16km)
No. of events
38.0
38.2
38.4
38.6
38.8
8.0
7.8
7.6
7.4
7.2
7.0

244

Figure 7 – Event locations and mixture distributions for varying levels of travel time error (1% top, 5% middle, 10% bottom) using velocity Model 1 from Fig 5. All velocity models produced similar results. Left: Individual event locations using NonLinLoc (blue circles). Black triangles are seismic stations. Histograms show the number of events located within a 0.05 degree bin (latitude and longitude) or 5 km bin (depth). Right: Corresponding mixture distributions for all event locations (and estimates of their complete posterior PDFs). Red scatter and corresponding density curves represent mixture distributions of NonLinLoc event location PDFs with respect to a given plane (latitude, longitude, depth).

6 Further Source Characteristics

There is some evidence of repeating event source(s) from high inter-event cross-correlation (CC) values (e.g., Augliera et al., 1995) at station C02E, the closest station to the study area, with 47 out of a total of 58 P-wave arrivals having CC values > 0.7 with at least one other event (4 sec window around P-wave arrival; at least 4 distinct multiplet groups identified). However, this is not seen at other stations across the two volcanic arrays, where inter-event CC values are consistently low due to low SNR, particularly across the Aluto array (on average, < 4 out of 58 events have CC value > 0.7 with at least one other event at a given station). As such, it is difficult to determine whether events have similar source mechanisms or exploit any self-similarity in our analyses of event locations.

Most events occur over a two-month period (Fig 8), with 45 of 58 events and 90 % of cumulative seismic moment (M_0) occurring during March and April 2012. M_0 and moment magnitudes (M_W) were calculated for each event at each station using spectral analysis of both P- and S-wave arrivals, with noise spectra subtracted, and Brune source model fitting (Abercrombie, 1995; Prejean & Ellsworth, 2001; Wilks, 2016). The values of M_0 and M_W were then averaged across all stations to attain a final, single value of M_0 and M_W for each event. To verify the quality of these predicted magnitude values, local magnitudes (M_L) were also calculated, using a scale calibrated for the MER (Keir et al., 2006), with station corrections (determined by the average deviation of magnitudes measured at a given station) applied to account for the variability in the recording environments from station to station. Estimates of M_L and M_W were found to be in close alignment, with the 2.5% and 97.5% quantiles for $M_L - M_W$ equal to -0.28 and 0.29, respectively. First motion polarities, where identified, for all events within the main cluster (January – June 2012) show a consistent trend: first motions across one array were consistently opposite to those at the other. During this period, first motion was predominantly downward (dilation) across the Corbetti stations and upward (compression) across the Aluto stations, although these polarities reversed to their opposite sign on at least three occasions. However, the final four isolated events (between August 2012 and May 2013) had distinctly different behavior: the polarities were the same across both arrays, with two events having compression first motion across all stations and the other two events having dilation first motion across all stations. This overall behavior is interesting, particularly as these events are clustered in time, as it suggests they may represent different sources or a complex pattern from a single process.

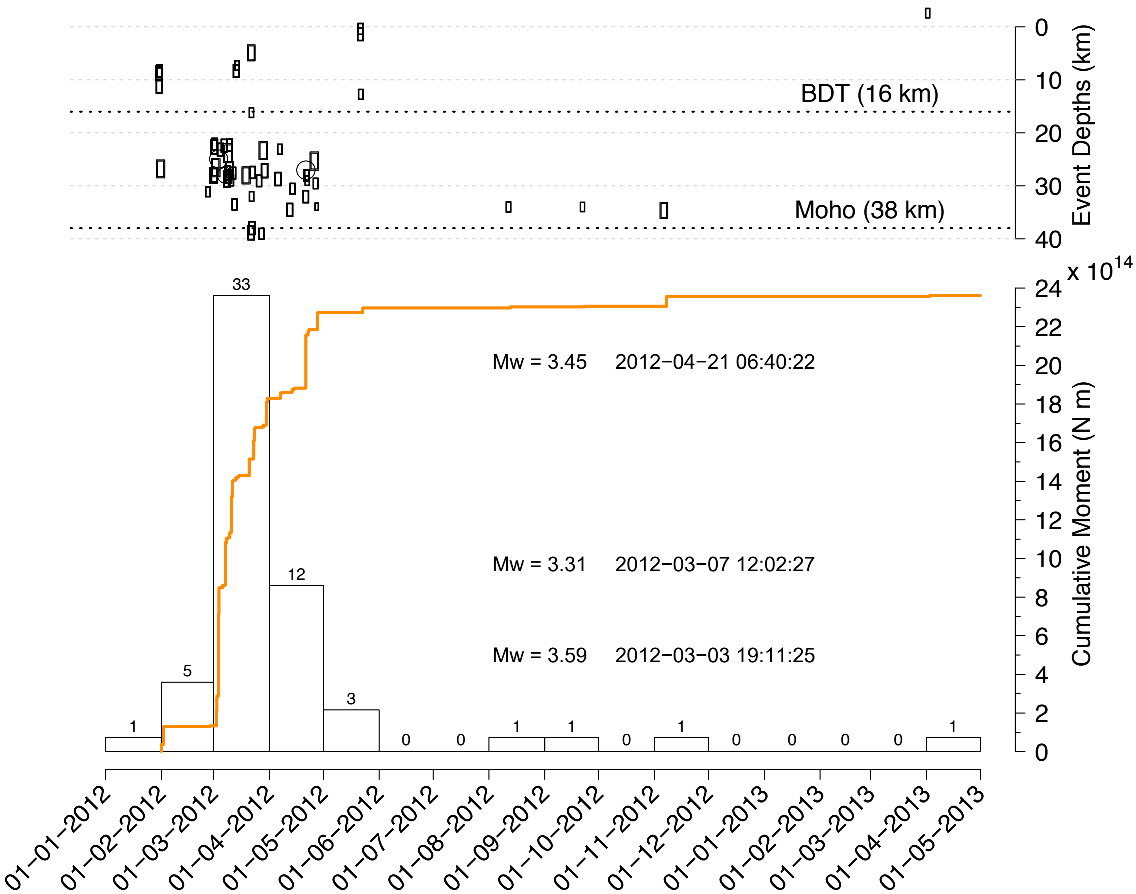

Figure 8 – Bottom: cumulative moment for all located events (orange line) and histogram of number of events per month (yellow). 90% of total moment occurred in March/April 2012. Largest three events and moment size indicated in blue. Top: Corresponding event depths (grey and blue circles) from Fig 7, TT (travel-time) error = 0.01. Moho depth of 38 km approximated from Dugda et al. (2005) *and Stuart et al*. (2006).

7 Discussion

Mixture distributions were used to overcome potential misinterpretations arising from large depth uncertainties in individual hypocentre locations and to assess the overall likelihood of lower crustal events. The overall mixture distribution mode and majority of maximum likelihood estimates (MLEs) for hypocentre locations lie between 25 and 35 km depth for all velocity models and levels of travel-time error (Fig 7). These results indicate that earthquakes beneath the magmatic MER and its border faults likely occur at lower crustal depths and far below the generally recognized seismogenic zone along the rift (Keir et al., 2009; Muluneh et al., 2018; Yang & Chen, 2010).

Our MLE hypocentre locations suggest a possible bimodal distribution of event depths (above 15km and below 20 km), which is consistent with depth distributions previously observed near the MER (Keir et al., 2009) and in less magmatic sections of the EAR (Yang & Chen, 2010). The ephemeral and very localized nature of this seismicity (Figs 7 and 8) combined with low event magnitudes (range: 1.9 – 3.6 M_W; median: 2.5 M_W), the magmatic setting associated with the Corbetti volcano and MER, and the adjacent hot springs around the Wondo Genet scarp at the surface all suggest that these lower crustal events are likely related to fluid or magmatic processes (Keir et al., 2009; Yang & Chen, 2010) rather than slip on cold or modified crust.

Seismicity in the area around Wondo Genet, where our mixture location distribution mode lies, has not been observed in previous (e.g., Maguire et al., 2003) or subsequent (e.g., Lavayssière, Greenfield, et al., 2019) seismic deployments, with the latter study deploying a broadband seismometer directly above the area of seismicity identified in this paper. This lack of subsequent seismicity supports the interpretation that these events were, in fact, related to a single, ephemeral intrusion or transient exsolution / migration of volatiles, rather than ongoing volcanic or shallow hydrothermal activity associated with the Corbetti caldera or Wondo Genet hot springs. A reasonable interpretation from the identified pattern of first motion polarities across the two arrays (Section 6) could be a stable source mechanism during the main period of an intrusion (i.e., the main cluster of events during Jan – April 2012) followed by a more complex process following the intrusion event. Alternatively, the transient presence of hot fluids may have increased pore pressure or reduced the effective normal stress on the border and cross-rift faults at this intersection. Unfortunately, additional assessments of source mechanism (e.g., focal mechanism determination / full waveform inversion) and relative event locations (e.g., double-differencing and coda wave interferometry) all yielded poor or unstable solutions due to the low number of events, large array gap, low number of picks / stations, unknown velocity model error, low SNR and low cross-correlation values. As such, assessment of source must come from temporal and spatial characteristics combined with plausible physical mechanisms within the regional setting.

The weakness of our analysis lies in the relative location of instruments available during the study period, which yields large depth errors for individual hypocentre locations regardless of velocity model or error estimates (Lomax et al., 2009). As such, it is impossible to state whether any of these events lie below the Moho, assumed to be at 37 – 40 km depth for the southern MER (Ayele et al., 2004; Dugda et al., 2005; Stuart et al., 2006), or whether they are all constrained within the lower crust. Stable overall population (mixture) distributions, however, reveal a clear mode between 28 and 32 km depth, regardless of velocity model or parameter adjustments, and thus strongly suggest that at least some of these events are deep. Whilst the highly heterogeneous composition beneath the rift and these volcanic centres makes it difficult, or even impossible, to know which level of error is most appropriate, an error level of no more than 10 % of travel-time seems suitable given the error bounds published for one of the regional velocity models used in this study (approx. 1.6 % difference in total travel-time; Daly et al., 2008) and the maximum absolute difference in travel-times between all models used (approx. 8 %).

One way in which our hypocentre location estimates could be placed artificially deep is through use of a velocity model that is slower than the true Earth velocity structure (e.g., Poliannikov & Malcolm, 2016). Where the velocity model used is incorrect, the direct-search approach of NonLinLoc provides a better estimate of location hypocentre than linearised methods, as negative and positive travel time residuals need not be balanced to produce a complete posterior probability distribution. By contrast, linearised approaches produce a single point estimate, often with Gaussian errors subsequently calculated (Gesret et al., 2015). It is possible to use approaches which jointly infer the velocity structure and event origin parameters to obtain PDFs of the hypocentre with the uncertainty of the velocity included (e.g., Piana Agostinetti et al., 2015), but these require either good coverage of the volume being imaged or well-constrained prior information on velocities to tightly locate events, which is not available here. Regardless, every care has been taken to use velocity models representative of the region through use of several previously published models (Daly et al., 2008; Mackenzie et al., 2005) and a range of travel time error levels that are consistent with other published estimates of velocity structure (e.g., Keranen et al., 2009). Furthermore, the previously identified magmatic-hydrothermal activity beneath Aluto and Corbetti volcanoes (Lloyd, Biggs, Birhanu, et al., 2018; Wilks et al., 2017) would suggest that the true Earth velocity structure along the ray path to these volcanic centres would more likely be slower, rather than faster, than our models, which do not incorporate any adjustments for these volcanic centres.

The source of lower crustal seismicity and processes by which magmatism evolves within the crust in continental rift zones remains an outstanding question (e.g., Weinstein et al., 2017). The 2012 – 2013 seismicity east of Corbetti volcano appears to lie at a potential intersection between the rift border and a pre-existing cross-rift structure beneath the Corbetti caldera (Lloyd, Biggs, Wilks, et al., 2018). However, the apparent NW-SE linear/listric distribution of events away from Corbetti is almost certainly an artefact of array geometry (Lomax et al., 2009), with the vast majority of individual location PDFs from NonLinLoc marking out this cross-rift 'trend', so it is impossible to say whether this seismicity relates to or indicates the easternmost extent of this cross-rift structure. Event locations near Corbetti do, however, fit with observations of lower crustal seismicity in other regions of recent volcanism, both around the MER (Keir et al., 2009) and other volcanic centres (e.g., Neuberg et al., 2006; Soosalu et al., 2010). The distance of the overall distribution mode of seismicity at ~ 30 km from the Corbetti caldera suggests that the source of these events is exploiting a potential point of weakness along the rift border fault or cross-rift structure rather than being directly related to the magmatic storage processes beneath Corbetti (Lloyd, Biggs, Birhanu, et al., 2018; Lloyd, Biggs, Wilks, et al., 2018). Plausible mechanisms, given the temporal and spatial distribution of this seismicity, include the movement of magma and/or exsolution of volatiles causing transient high strain rates and pore fluid pressures that induce seismicity (e.g., Greenfield & White, 2015; Keir et al., 2009; Soosalu et al., 2010) or reduce the effective normal stress on the border or cross-rift faults (e.g., Reyners et al., 2007), as opposed to an unusually strong lower crust (e.g., Craig et al., 2011). Further seismic monitoring, both in this area and of Ethiopian volcanoes in general, would provide greater opportunity to observe such lower crustal events again in the future, constrain source process and identify how magma migrates from mantle to crust in continental rift zones.

Acknowledgments, Samples, and Data

We would like to thank SEIS-UK for the use of their equipment, for their help while in the field and upon managing the data when back in the UK. Likewise, we thank various collaborators from the Ethiopian Electric Power Corporation (EEPCo) and the Geological Survey of Ethiopia (GSE) for their contributions to the project. The Bristol University Microseismic ProjectS (BUMPS) provided funding for the seismic experiment and fieldwork and the seismic equipment was loaned from SEIS-UK with GEF loan 962. The seismic network, XM, and the waveforms used in this study are open access and available through IRIS Data Services (http://service.iris.edu/fdsnws/dataselect/1/). See https://www.fdsn.org/networks/detail/XM_2012 for further details on data access and availability. Velocity models, phase arrival pick times, a catalog of events and an example link to download SAC waveform data through IRIS can be found in the Supplementary Material.

Author SL is supported by a GW4+ Doctoral Training Partnership studentship from the Natural Environment Research Council (NERC) [NE/L002434/1]. Author MW was funded by an EPSRC studentship and author KVC is supported by the AXA Research Fund and a Royal Society Wolfson Merit Award. Author AN was supported by NERC [NE/R001154/1, REMIS: Reliable Earthquake Magnitudes for Induced Seismicity]. This work is a contribution to the NERC funded RiftVolc project [NE/L013932/1, Rift volcanism: past, present and future].

References

Abercrombie, R. E. (1995). Earthquake source scaling relationships from -1 to 5 M_L using seismograms recorded at 2.5-km depth. *Journal of Geophysical Research*, *100*(B12), 24015–24036. https://doi.org/10.1029/95JB02397

Addison, P. S., Watson, J. N., & Feng, T. (2002). Low-oscillation complex wavelets. *Journal of Sound and Vibration*, *254*(4), 733–762. https://doi.org/10.1006/jsvi.2001.4119

Albaric, J., Déverchère, J., Perrot, J., Jakovlev, A., & Deschamps, A. (2014). Deep crustal earthquakes in North Tanzania , East Africa: Interplay between tectonic and magmatic processes in an incipient rift. *Geochemistry, Geophysics, Geosystems*, *15*(2), 374–394. https://doi.org/10.1002/2013GC005027

Augliera, P., Cattaneo, M., & Eva, C. (1995). Seismic multiplets analysis and its implication in seismotectonics. *Tectonphysics*, *248*, 219–234. https://doi.org/10.1016/0040-1951(94)00274-D

Ayele, A., Stuart, G., & Kendall, J.-M. (2004). Insights into rifting from shear wave splitting and receiver functions: an example from Ethiopia. *Geophysical Journal International*, *157*(1), 354–362. https://doi.org/10.1111/j.1365-246X.2004.02206.x

Chen, W., & Molnar, P. (1983). Focal depths of intracontinental and intraplate earthquakes and their implications for the thermal and mechanical properties of the lithosphere. *Journal of Geophysical Research: Solid Earth*, *88*(B5), 4183–4214. https://doi.org/10.1029/JB088iB05p04183

Craig, T. J., Jackson, J. A., Priestley, K., & McKenzie, D. (2011). Earthquake distribution patterns in Africa: their relationship to variations in lithospheric and geological structure, and their rheological implications. *Geophysical Journal International*, *185*, 403–434. https://doi.org/10.1111/j.1365-246X.2011.04950.x

Daly, E., Keir, D., Ebinger, C. J., Stuart, G. W., Bastow, I. D., & Ayele, A. (2008). Crustal tomographic imaging of a transitional continental rift: the Ethiopian rift. *Geophysical Journal International*, *172*(3), 1033–1048. https://doi.org/10.1111/j.1365-246X.2007.03682.x

Doser, D. I., & Yarwood, D. R. (1994). Deep crustal earthquakes associated with continental rifts. *Tectonophysics*, *229*, 123–131. https://doi.org/10.1016/0040-1951(94)90008-6

Dugda, M. T., Nyblade, A. A., Julia, J., Langston, C. A., Ammon, C. J., & Simiyu, S. (2005). Crustal structure in Ethiopia and Kenya from receiver function analysis: Implications for rift development in eastern Africa.

Journal of Geophysical Research: Solid Earth, *110*(B1), 1–15. https://doi.org/10.1029/2004JB003065

Ebinger, C. J., Keir, D., Bastow, I. D., Whaler, K., Hammond, J. O. S., Ayele, A., … Hautot, S. (2017). Crustal Structure of Active Deformation Zones in Africa: Implications for Global Crustal Processes. *Tectonics*, *36*, 3298–3332. https://doi.org/10.1002/2017TC004526

Foster, A. N., & Jackson, J. A. (1998). Source parameters of large African earthquakes: implications for crustal rheology and regional kinematics. *Geophysical Journal International*, *134*, 422–448. https://doi.org/10.1046/j.1365-246x.1998.00568.x

Fryzlewicz, P. (2014). Wild binary segmentation for multiple change-point detection. *Annals of Statistics*, *42*(6), 2243–2281. https://doi.org/10.1214/14-AOS1245

Gesret, A., Desassis, N., Noble, M., Romary, T., & Maisons, C. (2015). Propagation of the velocity model uncertainties to the seismic event location. *Geophysical Journal International*, *200*, 52–66. https://doi.org/10.1093/gji/ggu374

Greenfield, T., & White, R. S. (2015). Building icelandic igneous crust by repeated melt injections. *Journal of Geophysical Research: Solid Earth*, *120*, 7771–7788. https://doi.org/10.1002/2015JB012009

Hammond, J. O. S., Kendall, J.-M., Wookey, J., Stuart, G. W., Keir, D., & Ayele, A. (2014). Differentiating flow, melt, or fossil seismic anisotropy beneath Ethiopia. *Geochemistry, Geophysics, Geosystems*, *15*, 1878–1894. https://doi.org/10.1002/2013GC005185

Jackson, J., & Blenkinsop, T. (1993). The Malawi Earthquake of March 10, 1989: Deep Faulting within the East African Rift System. *Tectonics*, *12*(5), 1131–1139. https://doi.org/10.1029/93TC01064

Keir, D., Stuart, G. W., Jackson, A., & Ayele, A. (2006). Local Earthquake Magnitude Scale and Seismicity Rate for the Ethiopian Rift. *Bulletin of the Seismological Society of America*, *96*(6), 2221–2230. https://doi.org/10.1785/0120060051

Keir, D., Bastow, I. D., Whaler, K. A., Daly, E., Cornwell, D. G., & Hautot, S. (2009). Lower crustal earthquakes near the Ethiopian rift induced by magmatic processes. *Geochemistry, Geophysics, Geosystems*, *10*(6), 1–10. https://doi.org/10.1029/2009GC002382

Keir, D., Bastow, I. D., Corti, G., Mazzarini, F., & Rooney, T. O. (2015). The origin of along-rift variations in faulting and magmatism in the Ethiopian Rift. *Tectonics*, *34*, 464–477. https://doi.org/10.1002/2014TC003698

Kendall, J.-M., Stuart, G. W., Ebinger, C. J., Bastow, I. D., & Keir, D. (2005). Magma-assisted rifting in Ethiopia. *Nature*, *433*, 146–148. https://doi.org/10.1038/nature03161

Keranen, K. M., Klemperer, S. L., Julia, J., Lawrence, J. F., & Nyblade, A. A. (2009). Low lower crustal velocity across Ethiopia: Is the Main Ethiopian Rift a narrow rift in a hot craton? *Geochemistry, Geophysics, Geosystems*, *10*, 1–21. https://doi.org/10.1029/2008GC002293

Lapins, S., Roman, D. C., Rougier, J., De Angelis, S., Cashman, K. V, & Kendall, J.-M. (2020). An examination of the continuous wavelet transform for volcano-seismic spectral analysis. *Journal of Volcanology and Geothermal Research*, *389*, 106728. https://doi.org/10.1016/j.jvolgeores.2019.106728

Lavayssière, A., Drooff, C., Ebinger, C., Gallacher, R., Illsley-Kemp, F., Oliva, S. J., & Keir, D. (2019). Depth Extent and Kinematics of Faulting in the Southern Tanganyika Rift, Africa. *Tectonics*, (38), 842–862. https://doi.org/10.1029/2018TC005379

Lavayssière, A., Greenfield, T., Keir, D., Ayele, A., & Kendall, J.-M. (2019). Local seismicity near the actively deforming Corbetti volcano in the Main Ethiopian Rift. *Journal of Volcanology and Geothermal Research*, *381*, 227–237. https://doi.org/10.1016/j.jvolgeores.2019.06.008

Lindenfeld, M., & Rümpker, G. (2011). Detection of mantle earthquakes beneath the East African Rift. *Geophysical Journal International*, *186*(1), 1–5. https://doi.org/10.1111/j.1365-246X.2011.05048.x

Lloyd, R., Biggs, J., Wilks, M., Nowacki, A., Kendall, J.-M., Ayele, A., … Eysteinsson, H. (2018). Evidence for cross rift structural controls on deformation and seismicity at a continental rift caldera. *Earth and Planetary Science Letters*, *487*, 190–200. https://doi.org/10.1016/j.epsl.2018.01.037

Lloyd, R., Biggs, J., Birhanu, Y., Wilks, M., Gottsmann, J., Kendall, J.-M., … Eysteinsson, H. (2018). Sustained Uplift at a Continental Rift Caldera. *Journal of Geophysical Research: Solid Earth*, *123*, 5209–5226. https://doi.org/10.1029/2018JB015711

Lomax, A., Virieux, J., Volant, P., & Berge, C. (2000). Probabilistic earthquake location in 3D and layered models: Introduction of a Metropolis-Gibbs method and comparison with linear locations. In C. H. Thurber & N. Rabinowitz (Eds.), *Advances in Seismic Event Location* (pp. 101–134). Asterdam: Kluwer.

Lomax, A., Michelini, A., & Curtis, A. (2009). *Earthquake Location, Direct, Global-Search Methods*. (R. A. Meyers, Ed.), *Complexity In Encyclopedia of Complexity and System Science* (Part 5). New York, NY: Springer New York. https://doi.org/10.1007/978-0-387-30440-3

Mackenzie, G. D., Thybo, H., & Maguire, P. K. H. (2005). Crustal velocity structure across the Main Ethiopian Rift:

results from two-dimensional wide-angle seismic modelling. *Geophysical Journal International*, *162*(3), 994–1006. https://doi.org/10.1111/j.1365-246X.2005.02710.x

Maguire, P. K. H., Ebinger, C. J., Stuart, G. W., Mackenzie, G. D., Whaler, K. A., Kendall, J.-M., … Abebe, B. (2003). Geophysical Project in Ethiopia Studies Continental Breakup. *Eos Trans. AGU*, *84*(35), 337–343. https://doi.org/10.1029/2003EO350002

Muluneh, A. A., Kidane, T., Corti, G., & Keir, D. (2018). Constraints on fault and crustal strength of the Main Ethiopian Rift from formal inversion of earthquake focal mechanism data. *Tectonophysics*, *731–732*(February), 172–180. https://doi.org/10.1016/j.tecto.2018.03.010

Muluneh, A. A., Cuffaro, M., & Kidane, T. (2017). Along-strike variation in deformation style inferred from kinematic reconstruction and strain rate analysis: A case study of the Ethiopian Rift. *Physics of the Earth and Planetary Interiors*, *270*, 176–182. https://doi.org/10.1016/j.pepi.2017.07.009

Neuberg, J. W., Tuffen, H., Collier, L., Green, D., Powell, T., & Dingwell, D. (2006). The trigger mechanism of low-frequency earthquakes on Montserrat. *Journal of Volcanology and Geothermal Research*, *153*(1–2), 37–50. https://doi.org/10.1016/j.jvolgeores.2005.08.008

Nyblade, A. A., & Langston, C. A. (1995). East African earthquakes below 20 km depth and their implications for crustal structure. *Geophysical Journal International*, *121*(1), 49–62. https://doi.org/10.1111/j.1365-246X.1995.tb03510.x

Piana Agostinetti, N., Giacomuzzi, G., & Malinverno, A. (2015). Local three-dimensional earthquake tomography by trans-dimensional Monte Carlo sampling. *Geophysical Journal International*, *201*, 1598–1617. https://doi.org/10.1093/gji/ggv084

Poliannikov, O. V, & Malcolm, A. E. (2016). The effect of velocity uncertainty on migrated reflectors: Improvements from relative-depth imaging. *Geophysics*, *81*(1), S21–S29. https://doi.org/10.1190/geo2014-0604.1

Prejean, S. G., & Ellsworth, W. L. (2001). Observations of Earthquake Source Parameters at 2 km Depth in the Long Valley Caldera, Eastern California. *Bulletin of the Seismological Society of America*, *91*(2), 165–177. https://doi.org/10.1785/0120000079

Reyners, M., Eberhart-Phillips, D., & Stuart, G. (2007). The role of fluids in lower-crustal earthquakes near continental rifts. *Nature*, *446*, 1075–1078. https://doi.org/10.1038/nature05743

Smith, K. D., Kent, G. M., von Seggern, D. P., Driscoll, N. W., & Eisses, A. (2016). Evidence for Moho-lower crustal transition depth diking and rifting of the Sierra Nevada microplate. *Geophysical Research Letters*, *43*, 10738–10744. https://doi.org/10.1002/2016GL070283

Soosalu, H., Key, J., White, R. S., Knox, C., Einarsson, P., & Jakobsdóttir, S. S. (2010). Lower-crustal earthquakes caused by magma movement beneath Askja volcano on the north Iceland rift. *Bulletin of Volcanology*, *72*, 55–62. https://doi.org/10.1007/s00445-009-0297-3

Stuart, G. W., Bastow, I. D., & Ebinger, C. J. (2006). Crustal structure of the northern Main Ethiopian Rift from receiver function studies. *Geological Society, London, Special Publications*, *259*, 253–267. https://doi.org/10.1144/GSL.SP.2006.259.01.20

Weinstein, A., Oliva, S. J., Ebinger, C. J., Roecker, S., Tiberi, C., Aman, M., … Fischer, T. P. (2017). Fault-magma interactions during early continental rifting: Seismicity of the Magadi-Natron-Manyara basins, Africa. *Geochemistry, Geophysics, Geosystems*, *18*(10), 3662–3686. https://doi.org/10.1002/2017GC007027

White, R. S., Drew, J., Martens, H. R., Key, J., Soosalu, H., & Jakobsdóttir, S. S. (2011). Dynamics of dyke intrusion in the mid-crust of Iceland. *Earth and Planetary Science Letters*, *304*(3–4), 300–312. https://doi.org/10.1016/j.epsl.2011.02.038

Wilks, M. (2016). *A Seismological Investigation into Tectonic, Magmatic and Hydrothermal Processes at Aluto and Corbetti, Two Restless Volcanoes in the Main Ethiopian Rift* (Doctoral thesis). University of Bristol.

Wilks, M., Kendall, J.-M., Nowacki, A., Biggs, J., Wookey, J., Birhanu, Y., … Bedada, T. (2017). Seismicity associated with magmatism, faulting and hydrothermal circulation at Aluto Volcano, Main Ethiopian Rift. *Journal of Volcanology and Geothermal Research*, *340*, 52–67. https://doi.org/10.1016/j.jvolgeores.2017.04.003

Withers, M., Aster, R., Young, C., Beiriger, J., Harris, M., Moore, S., & Trujillo, J. (1998). A comparison of select trigger algorithms for automated global seismic phase and event detection. *Bulletin of the Seismological Society of America*, *88*(1), 95–106.

Wolfenden, E., Ebinger, C., Yirgu, G., Deino, A., & Ayalew, D. (2004). Evolution of the northern Main Ethiopian rift : birth of a triple junction. *Earth and Planetary Science Letters*, *224*, 213–228. https://doi.org/10.1016/j.epsl.2004.04.022

Yang, Z., & Chen, W.-P. (2010). Earthquakes along the East African Rift System: A multiscale, system-wide perspective. *Journal of Geophysical Research: Solid Earth*, *115*(B12), 1–31. https://doi.org/10.1029/2009JB006779

Zhao, M., Langston, C. A., Nyblade, A. A., & Owens, T. J. (1997). Lower-crustal rifting in the Rukwa Graben, East Africa. *Geophysical Journal International*, *129*(2), 412–420. https://doi.org/10.1111/j.1365-246X.1997.tb01592.x